Electronic Supplementary Material (ESI) for Journal of Materials Chemistry A.

Electronic Supplementary Information

Unravelling the structural complexity and photophysical properties of adamantyl-based layered hybrid perovskites

Farzaneh Jahanbakhshi,[#a] Marko Mladenović,[#a] Ekaterina Kneschnaurek,[#b] Lena Merten,[b] María C. Gélvez-Rueda,[c] Paramvir Ahlawat,[a] Yang Li,[d] Algirdas Dučinskas,[d] Alexander Hinderhofer,[b] M. Ibrahim Dar,[d] Wolfgang Tress,[e] Brian Carlsen,[e] Amita Ummadisingu,[d] Shaik M. Zakeeruddin,[d] Anders Hagfeldt,[e] Frank Schreiber,[b] Ferdinand C. Grozema,[c*] Ursula Rothlisberger,[a*] Jovana V. Milić,[d*] and Michael Graetzel[d*]*

[a]Laboratory of Computational Chemistry and Biochemistry, EPFL, Switzerland.
[b]Soft Matter Physics, University of Tuebingen, Germany.
[c]Delft University of Technology, The Netherlands.
[d]Laboratory of Photonics and Interfaces, EPFL, Lausanne, Switzerland.
[e]Laboratory of Photomolecular Science, EPFL, Lausanne, Switzerland.

Table of Contents

S1. Materials and Methods

Perovskite mechanosynthesis: Perovskite powders were synthesized by grinding the reactants in an electric ball mill (Retsch Ball Mill MM-200 using a grinding jar (10 ml) and a ball (⌀10 mm) for 30 min at 25 Hz. The resulting powders were annealed at 150 °C for 15 min to reproduce the thin film synthetic procedure, in accordance with previously reported procedures.[1–3] The amounts of reagents taken into the synthesis were determined by the reported (nominal) stoichiometry.

Thin Film Preparation: Films were fabricated through a stepwise preparation process reported previously.[3] The quartz substrates were cleaned with oxygen plasma for 15 min. The perovskite film was deposited by spin-coating onto the substrate. The precursor solutions of the $A_2FA_{n-1}Pb_nI_{3n+1}$ and $A'_2FA_{n-1}Pb_nI_{3n+1}$ perovskite films (n = 1, 2, 3; FA = formamidinium) of the concentration of 0.4 M were prepared in a nitrogen-filled glovebox by dissolving the stoichiometric quantities of PbI_2, FAI, and either (1-adamantyl)methanammonium iodide (ADAMI, AI) or 1-adamantylammonium iodide (ADA, A'I) in the solvent mixture comprised of *N*,*N*-dimethylformamide (DMF) and dimethyl sulfoxide (DMSO) with the volume ratio of DMF/DMSO = 4:1. The perovskite film spin-coating procedure was performed in a glovebox under inert nitrogen atmosphere by a consecutive two-step spin-coating process at first 1000 rpm for 10 s with a ramp of 200 rpm s^{-1} and second 4000 rpm for 20 s with a ramp of 2000 rpm s^{-1}. Subsequently, the substrate was annealed at 150 °C for 20 min.

X-ray diffraction (XRD) spectra were recorded on an X'Pert MPD PRO (PANanalytical) equipped with a ceramic tube providing Ni-filtered (Cu anode, λ = 1.54060 Å) radiation and a RTMS X'Celerator (PANalytical). The measurements were done in Bragg-Brentano geometry from 2Θ = 5–60 °. The samples were mounted without further modification and the automatic divergence slit (10 mm) and beam mask (10 mm) were adjusted to the dimension of the films. The XRD patterns of these materials have been reported previously.[3] Schematic representations are generated by VESTA.[4]

UV-Vis absorption spectral measurements were recorded using Varian Cary5 UV–visible spectrophotometer. The UV-Vis spectra of these materials have been reported previously.[3]

X-ray scattering experiments were done at beamline ID10 of the ESRF with a photon energy of 22 keV under nitrogen atmosphere. As a calibrant for the scattering experiments, LaB_6 was used. The sample-detector distance was 295 mm, while the beam size was 20 µm in vertical direction and 120 µm in horizontal direction. GIXD data was measured under an angle of incidence of 0.12° with a Cyberstar point detector. GIWAXS data was measured with a PILATUS 300k area detector under angles of incidence between 0.02°–0.20°. Powder diffraction data was calculated with Mercury. Scattering data analysis was performed with self-written Python and Matlab-based software.

S2. Supplementary Structural Data

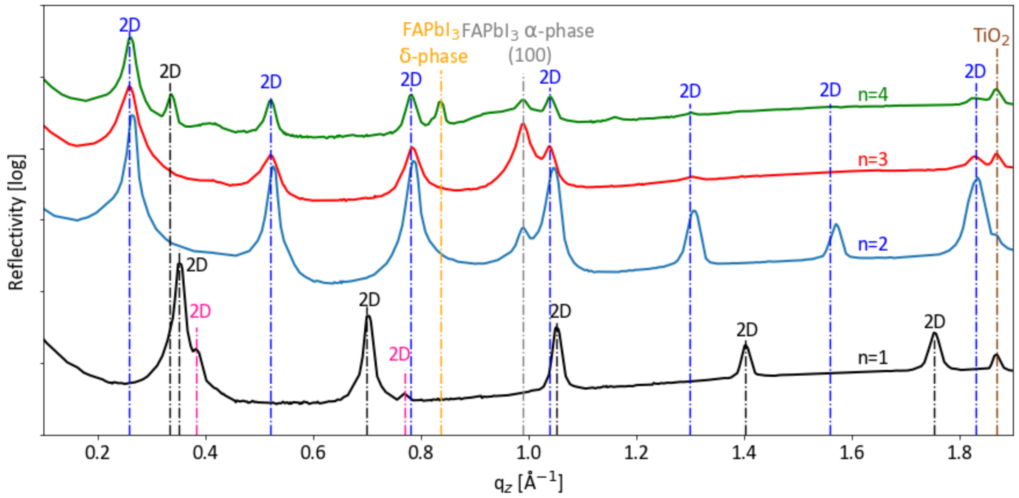

Figure S1. XRR patterns of $A_2FA_{n-1}Pb_nI_{3n+1}$ layered perovskite thin films on FTO/mp-TiO_2 substrates based on nominal *n* = 1–4 compositions. Characteristic signals for $FAPbI_3$ polymorphs (α-$FAPbI_3$ and δ-$FAPbI_3$ phases) are indicated as well.

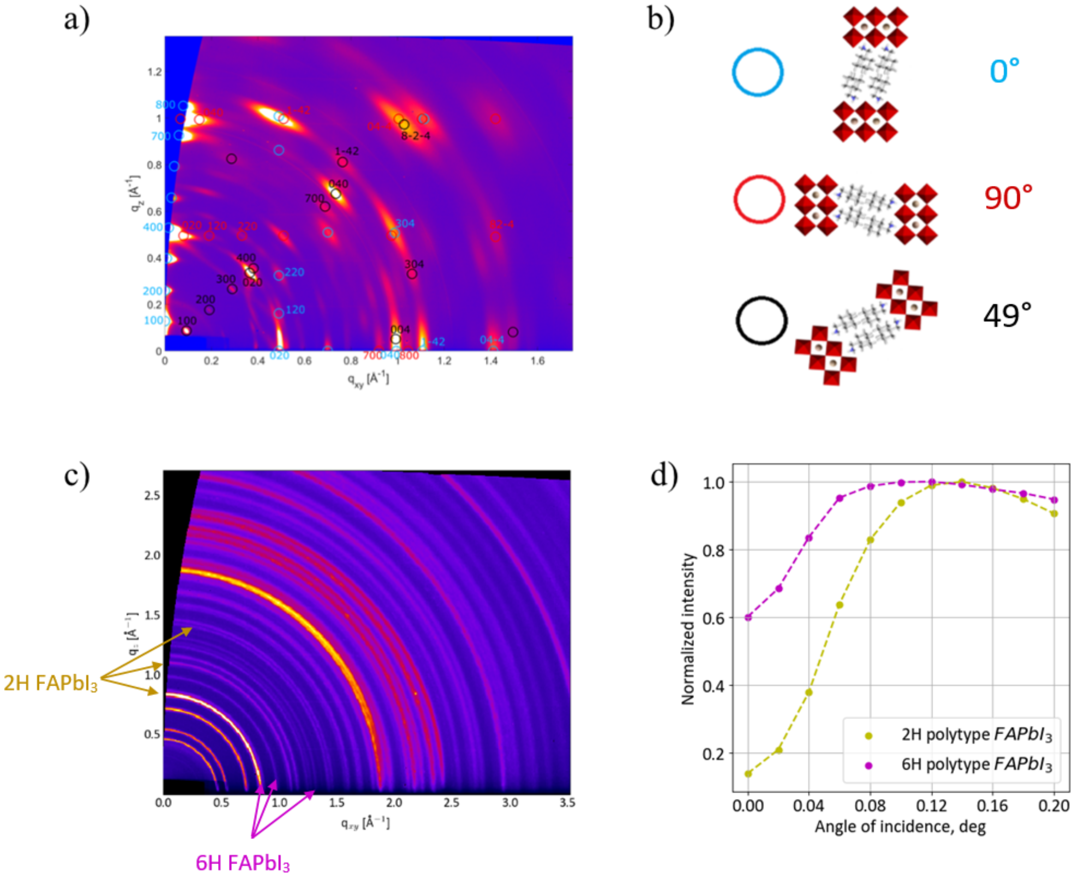

Figure S2. GIWAXS data for $A_2FA_2Pb_3I_{10}$ (*n* = 3 composition) thin films on FTO/mp-TiO_2 substrates with three different orientations of $A_2FAPb_2I_7$ (*n* = 2) structure: (a) initial image with indices and (b) representation of the orientations (0°, 90°, 49° tilt relative to the substrate normal). GIWAXS data of (c) $A'_2FA_2Pb_3I_{10}$ (*n* = 3) composition, angle of incidence was 0.20°. (d) Integrated intensities of 2H and 6H $FAPbI_3$ polytypes for this sample.

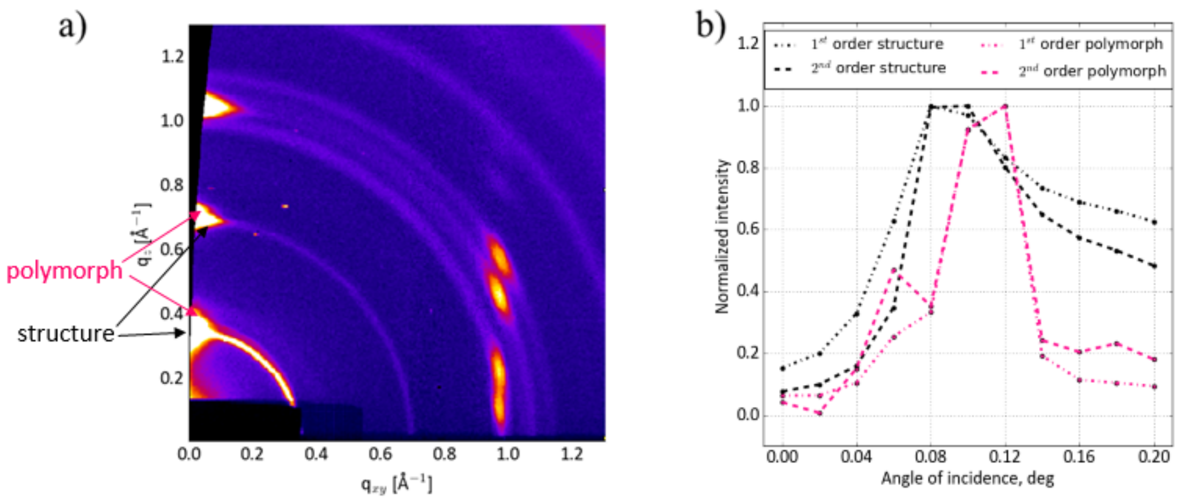

Figure S3. GIWAXS data for A_2PbI_4 (n = 1) composition thin films on FTO/mp-TiO_2 substrates with A_2PbI_4 (n = 1) layered 2D structure and the corresponding 2D polymorph. (a) Initial GIWAXS image with marked reflections, angle of incidence was 0.12°. (b) Integrated intensities of A_2PbI_4 (n = 1) layered 2D structure and the corresponding polymorph for this sample as a function of incidence angle.

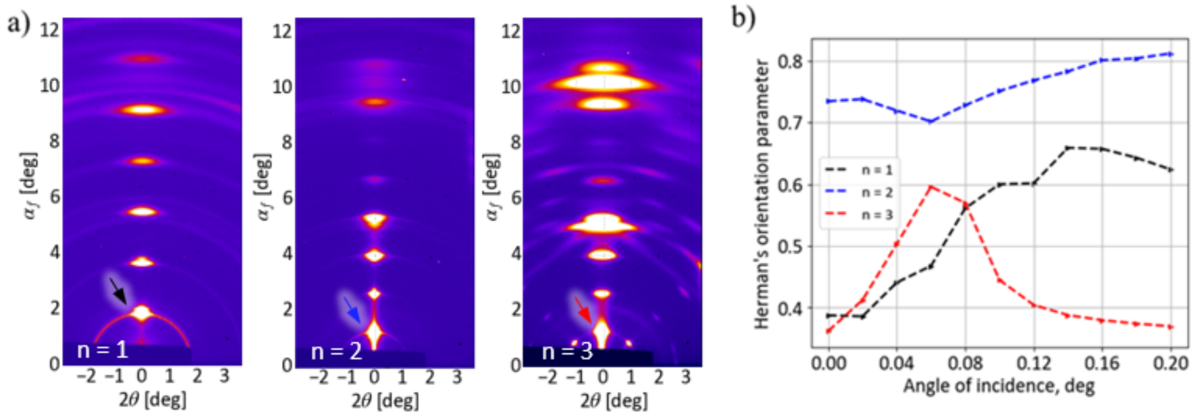

Figure S4. Angular space GIWAXS data of $A_2FA_{n-1}Pb_nI_{3n+1}$ (n = 1,2 and 3) composition thin films on FTO/mp-TiO_2 substrates. (a) GIWAXS data at angle of incidence 0.12°. (b) Calculated Herman's orientation parameter of the first order reflections (indicated with arrows) as a function of incidence angle. For the n = 1 composition, orientation analysis was performed for the n = 1 structure, while for n = 2 and n = 3 nominal compositions, the analysis was done for the n = 2 structure.

Table S1. Triclinic lattice parameters derived from fitting of GIWAXS data of the 2D structure of perovskites for $A_2FA_{n-1}Pb_nI_{3n+1}$ (n = 1–2) perovskite compositions, starting from DFT (PBEsol+D2-optimized) calculated values.

***n* = 1**	***a* [Å]**	***b* [Å]**	***c* [Å]**	**α [°]**	**β [°]**	**χ [°]**	***V* [Å^3]**
DFT	18.426	12.094	11.624	88.17	94.00	98.95	2549.332
Optimized	18.005	12.756	12.677	89.5	95.89	97	2874.57
Deviation [%]	-2.284	5.476	9.059	1.513	2.016	-1.972	12.758
***n* = 2**	***a* [Å]**	***b* [Å]**	***c* [Å]**	**α [°]**	**β [°]**	**χ [°]**	***V* [Å^3]**
DFT	24.396	12.094	11.881	87.17	93.64	97.47	3462.190
Optimized	24.100	12.678	12.645	89.45	95.9	97	3814.422
Deviation [%]	-0.803	4.832	6.430	2.616	2.415	-0.482	10.174

Table S2. Reflections and their higher orders based on the XRR data for $A_2FA_{n-1}Pb_nI_{3n+1}$ (n = 1–4) compositions. All q_z-values are given in Å^{-1}.

Legend	***n* = 1**	***n* = 2**	***n* = 3**	***n* = 4**
n = 1 structure *n* = 1 polymorph in the *n* = 1 composition *n* = 2 structure 3D perovskite $FAPbI_3$ 3D hexagonal $FAPbI_3$ TiO_2		0.265	0.259	0.262
	0.353			0.337
	0.384			
		0.526	0.521	0.522
	0.703			
	0.770			
		0.788	0.785	0.783
				0.837
		0.991	0.991	0.991
		1.048	1.040	1.041
	1.053			
	1.144			
		1.308	1.301	1.304
	1.404			
		1.571	1.576	1.562
	1.754			
		1.833	1.829	1.830
	1.878	1.878	1.878	1.878

S2.1. Herman's orientation analysis

Orientation analysis (Figure S4) was performed using Herman's orientation function to calculate the Herman's orientation parameter (f). The orientation parameter is defined as:

$$f = \frac{1}{2}(3\langle cos^2\varphi\rangle - 1)$$

where the average $\cos^2$ weighted by the intensity as a function of azimuthal angle (φ) is calculated as follows:

$$\langle cos^2\varphi\rangle = \frac{\int_0^{\frac{\pi}{2}} I(\varphi,\theta) sin\varphi \cdot cos^2\varphi d\varphi}{\int_0^{\frac{\pi}{2}} I(\varphi,\theta) sin\varphi d\varphi}$$

For perfect orientation in φ = 0 direction (*face-on*), f would adopt a value of 1, while f = 0 would represent *random* orientation and f = -1/2 would indicate for a perfect orientation normal to φ = 0 (*side-on*, *parallel to the substrate*). Accordingly, the direction of φ = 0 was chosen along the q_z axis. The highest degree of orientation was observed for the n = 2 layered structure in the n = 2 composition, featuring an orientation parameter of around f = 0.8 (Figure S4). For the n = 1 structure in samples with n = 1 composition, Herman's orientation parameter increased with increasing angle of incidence, suggesting a higher degree of order towards the bulk of the film compared to the surface, reaching a maximum value just above f = 0.6. On the other hand, in the nominal n = 3 composition samples, where the orientation parameter was calculated for the n = 2 structure, it exhibited a maximum value of around 0.6 near the film surface, while decreasing towards the bulk.

S3. Molecular Dynamics Simulations

S3.1. Methods

Supercells are made of 120 stoichiometric units and the initial structures were built with VMD by placing the organic spacers between layers of Pb-I octahedra. A fixed-point charge interatomic potential was chosen for Pb and I from the available literature.[5] We have selected this force field because it is known to represent the crystal structures of both PbI_2 and perovskites. The structure and dynamics of PbI_2 is highly important in lead halide perovskites and this force field is known to capture the dynamics of edge-sharing Pb-I octahedra. The Generalized Amber Force Field (GAFF) was used to parameterize the spacer and formamidinium ions. We have chosen a 1.0 nm cutoff for nonbonded interactions and three-dimensional periodic boundary conditions were applied for each simulation. Long-range electrostatic interactions are treated with the particle-particle-particle-mesh Ewald method. We employ the SHAKE algorithm[6] to constrain the bond length of hydrogen atoms. The time step used in all of the simulations is 2 fs. All simulations are performed with the Large-scale Atomic/Molecular Massively Parallel Simulator (LAMMPS) code (31 Mar 2017).[7] The systems were first minimized with a conjugate gradient algorithm with a tolerance of maximum residual force of 10^{-3} kcal/mol A. After minimization, the systems were relaxed with an equilibrium run which was carried out in the isothermal-isobaric ensemble. We use a velocity rescaling thermostat[8] with a relaxation time of 0.1 ps. The Parrinello-Rahman barostat[9] was used to keep the pressure equal to the standard atmospheric pressure. The relaxation time of the triclinic variable cell barostat was set to 10 ps. We use the triclinic variable cell barostat in all of our simulations. With this setup, the temperature was slowly increased from 0 K to T (temperature, K) in 10 ns. Then we perform 30 ns simulations at the constant temperature. To calculate the autocorrelation function (ACF), we perform molecular dynamics (MD) simulations for five different temperatures (at 200 K, 250 K, 300 K, 350 K and 400 K). These simulations were run to verify the stability and calculations of rotational dynamics at different temperatures. In order to obtain the final structure, we quench it to 0 K.

S3.2. Initial Structure Analysis

Atomistic simulations are a widely used and established techniques to model the crystal structures of different complex compounds such as molecular crystals, metal alloys, oxide perovskites and many more. Since the configurational space for such a multicomponent system can be very vast, we perform experimental information-based MD simulations in perovskite configurational space. Two-dimensional lead halide perovskites are known to have mainly Dion-Jacobson (DJ) or Ruddlesden-Popper (RP) structures or structural analogues of these types. We start from building a DJ structure from corner-sharing Pb-I octahedra for a given perovskite configuration with organic spacers between these layers, since a DJ structure is more straightforward to build as compared to other structure types, such as RP. The initial structures of $A_2FA_{n-1}Pb_nI_{3n+1}$ perovskite systems with (1-adamantyl)methanammonium (ADAM, A) spacers of *n* = 1, 2 compositions are shown in Figure S5.

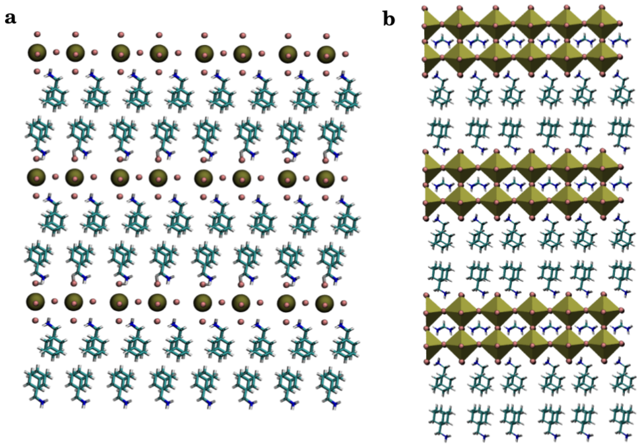

Figure S5. Initial structures of $A_2FA_{n-1}Pb_nI_{3n+1}$ perovskite system of *n* = 1 and *n* = 2 compositions. The supercell for initially built (a) *n* = 1 and (b) *n* = 2 compositions. Lead (Pb^{2+}) ions are shown with golden spheres, while iodide (I^-) ions are displayed with pink spheres. Pb–I octahedra are shown in golden. A = ADAM spacer and formamidinium (FA) ions are illustrated with a ball-and-stick model. Images are generated with the VMD.

S3.2. Analysis of the ADAM-based Perovskite Systems

We perform classical MD simulations of the initial structure (shown in Figure S5) in accordance with the procedure described in the Methods section. Following a slow gradual increase in temperature, we observe that the structure changes to the RP type and remains in this phase during the remaining 30 ns of the simulation. This is shown in Figure S6 and the movies SM-A1. The simulations show that the RP phase has a stable minimum on the potential energy surface, in contrast to the DJ structure.

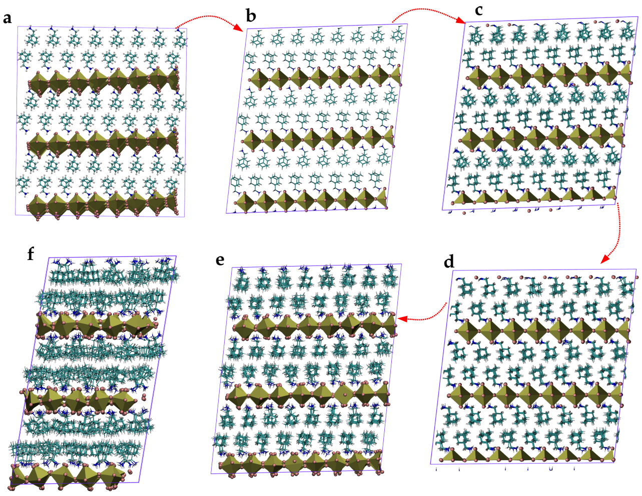

Figure S6. Structural changes of the A_2PbI_4 system (*n* = 1 composition) with increasing temperature. Lead (Pb^{2+}) ions are shown with golden spheres, while iodide (I^-) ions are displayed with pink spheres. Pb–I octahedra are shown in golden. Spacer A = ADAM and FA ions are illustrated with a ball-and-stick model. Images are generated with the VMD software.[10] f) is the side view of e) at 298 K, while d) is taken at 150 K.

Furthermore, we also found that the temperature has a significant effect on other structural properties (Figure S7). We show the evolution of the structure with the increase in temperature (Figure S6). We observe that there is a transition in the conformation of the spacer (e.g. from Figure S6d to Figure S6e). We find that the spacers are well aligned parallel to each other at lower temperatures (for instance, at 150 K shown in Figure S6d). However, at higher temperature (for instance, 298 K in Figure S6e) the carbocyclic core and the ammonium termini start to rotate around the backbone of the spacer (Figure S6f). These rotations can also be seen in the supplementary movies (SM-A1). For a quantitative assessment, we have calculated the angular autocorrelation function (ACF) of the orientation of spacer ADAM $\langle \hat{v}(t) \cdot \hat{v}(0) \rangle (\hat{v} = (\vec{r}_{C8} - \vec{r}_{C3})/(|\vec{r}_{C8} - \vec{r}_{C3}|))$ based on the equation (1)

$$ACF(t_\theta) = \langle \hat{v}(t).\hat{v}(0) \rangle = \frac{1}{N}\sum_{i=1}^{N}\frac{1}{M}\sum_{\theta=1}^{M}\hat{v}_i(t+t_\theta).\hat{v}_i(t) \qquad (1)$$

where $\vec{r}_{C8}$ and $\vec{r}_{C3}$ are positions of atoms C8 and C3 of the spacer A (as depicted in Figure S7).

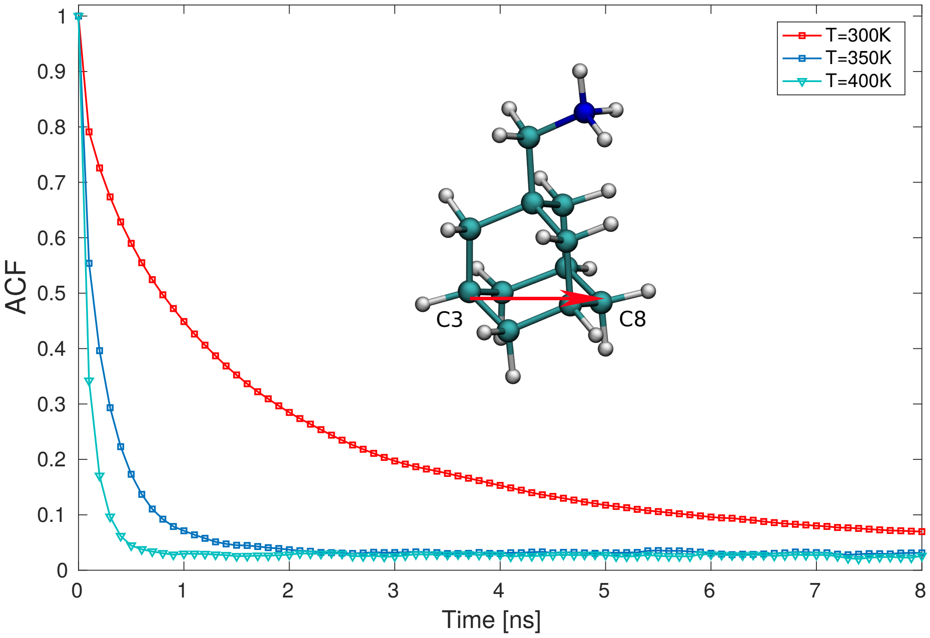

Figure S7. Time dependent autocorrelation function of the unit C3–C8 vectors of the spacer A. Image displays the decay of the ACF at different temperatures: 300 K, 350 K and 400 K for *n* = 1 compositions.

Importantly, the rotational times of the spacer are of the order of *ns*, which is in qualitative agreement with the time scale of the spacer dynamics observed in the NMR studies.[3] Similar simulations were performed for *n* = 2, *n* = 3 and *n* = 4 with comparable findings, i.e. that the most stable phase is an RP configuration, as expected (supplementary movies SM-A2, SM-A3 and SM-A4). Supplementary movies are deposited on Zenodo (doi.org/10.5281/zenodo.3982321).

S3.3. Analysis of ADA-based Perovskite Systems

To assess the role of the methylene linker in the ADAM-based systems, we also analyse the properties of the 2D systems based on 1-adamantylammonium (ADA) spacers. We follow a similar procedure as described in the previous subsection. We start from an initial DJ geometry and find that the structure changes to RP as the stable phase (shown in supplementary movie SM-A1). Structural differences between ADAM (A) and ADA (A') systems are apparent - there is a significant mutual tilt between adjacent Pb-I octahedra with A' that is either absent or less pronounced for spacer A. This behaviour has also been observed in other studies of rigid spacers. Furthermore, due to the higher rigidity of spacer A', the orientation of the spacer is more random (as shown in Figure S8).

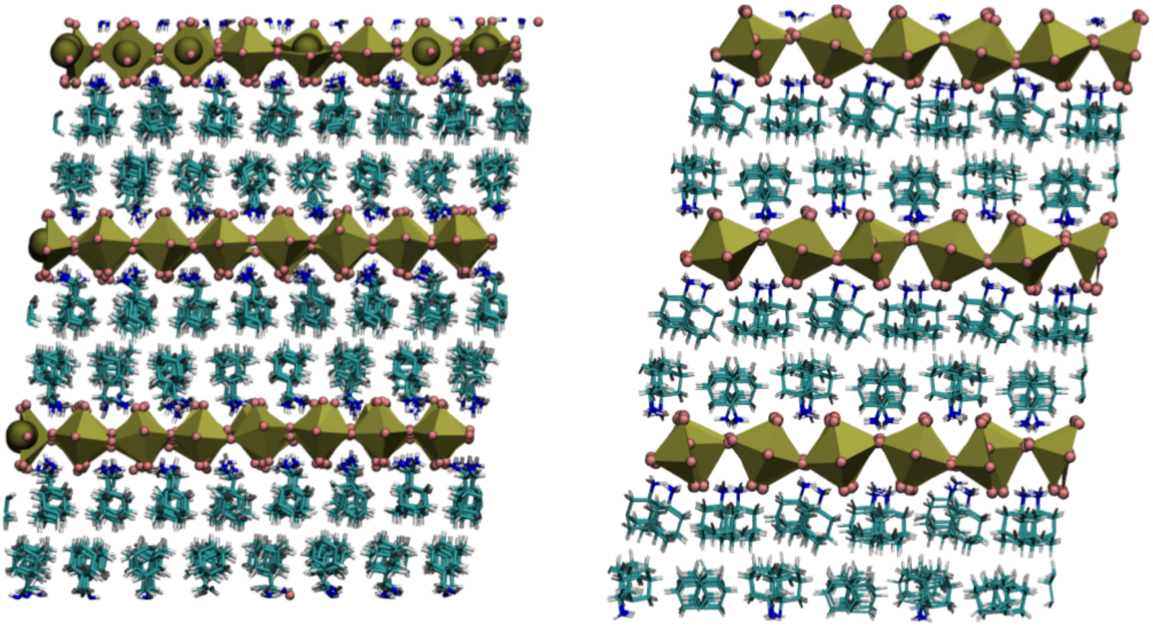

Figure S8. Comparison of equilibrated structures for ADAM (left) and ADA (right) layered perovskites (*n* = 1). Lead (Pb^{2+}) ions are shown with golden spheres, while iodide (I^{-}) ions are displayed with pink spheres. Pb–I octahedra are shown in gold. Spacer ADAM and formamidinium (FA) ions are illustrated with a ball-and-stick model. Images are generated with VMD.

S4. DFT Calculations

S4.1. Methods

Ab initio calculations based on the Generalized Gradient Approximation (GGA) of Density Functional Theory (DFT) for $A_2FA_{n-1}Pb_nI_{3n+1}$ and $A'_2FA_{n-1}Pb_nI_{3n+1}$ (n = 1, 2 and 3) were performed using the Quantum Espresso package.[11] The Perdew–Burke–Ernzerhof functional revised for solids (PBEsol)[12] was selected, which has shown to well reproduce measured electronic and structural properties of RP phases, such as the recently reported $AVA_2MA_{n-1}Pb_nI_{3n+1}$ systems.[13-14] Dispersion interactions were taken into account by applying the empirical D2 dispersion correction in order to obtain structural properties (reported in Table S1).[15] To calculate the band gaps, we employed a higher level of theory by applying the PBE0 functional together with incorporating spin-orbit coupling (SOC) effects.[16-17] Valence-core electron interactions were modelled via ultrasoft pseudopotentials with a plane wave basis set of 40 Ry kinetic energy cutoff for the wavefunction and 280 Ry for the density. The Brillouin zone was sampled by a 2×2×1 k-point grid for all cases. A finite temperature (FT) analysis was carried out by performing 5 *ps* of constant volume (NVT) Born-Oppenheimer molecular dynamics (MD) for A_2PbI_4 and A'_2PbI_4, excluding the first 1 *ps* of equilibration. The initial temperature was set to 300 K and was controlled by the velocity rescaling thermostat implemented in Quantum Espresso.[11] The same Brillouin zone sampling as in the static calculations was adopted for MD simulations. Charge carrier effective masses were calculated using our in-house code.[18] Formation energies were calculated by comparing the enthalpic contributions to free energy of the products ($A_2FA_{n-1}Pb_nI_{3n+1}$ and $A'_2FA_{n-1}Pb_nI_{3n+1}$ for n = 1–3) and the reactants (PbI_2, FAI, and AI/A'I).

S4.2. Structural Properties

To characterize the structural templating role of A and A' (Figure S9), we probed the penetration depths of the spacers into the inorganic slabs, which we recently reported as an indicator of octahedral tilting in RP and DJ phases of $AVA_2MA_{n-1}Pb_nI_{3n+1}$ (Tables S3–S4).[13–14,19]

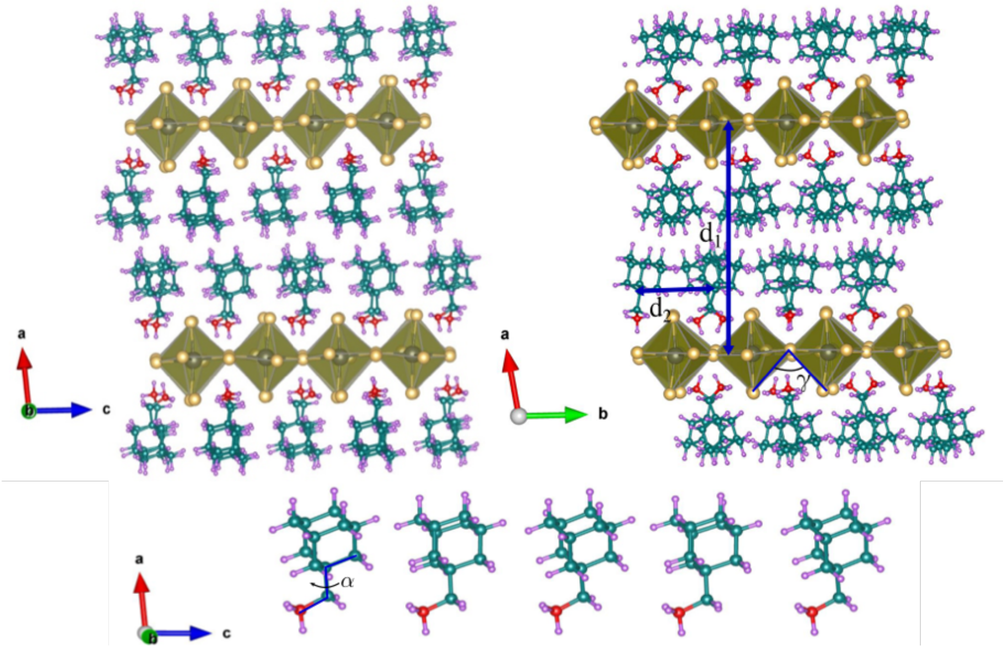

Figure S9. DFT (PBEsol)-optimized structures of A_2PbI_4 (left) and A'_2PbI_4 (right). Definition of some characteristic structural parameters: d_1, d_2, α and γ are indicated. The stacking of spacers is highlighted in the zoomed-in inset below.

Table S3. Characteristic structural features of PBEsol-optimized $A_2FA_{n-1}Pb_nI_{3n+1}$ for n = 1, 2 and 3. Octahedral tilting angles were measured with respect to two in-plane and one out-of-plane directions. Distances are given in Å. Dihedral angles of octahedral tilting angles and corresponding standard deviations are given in degrees. Values for d_1 for PBEsol + D2-optimized structures are given in brackets.

n	Octahedral Tilting (°)	N···Pb (Å)	N···I (Å)	d_1(Å)	d_2(Å)	α(˚)
1	123.3 ± 1.0, 121.9 ± 9.1, -	2.8	4.0	19.0 (18.2)	6.1	55.5 ± 1 0.1
2	115.4 ± 4.5, 114.3 ± 4.8, 94.4 ± 14.2	2.8	3.9	19.8 (17.7)	6.1	55.4 ± 7.3
3	105.2 ± 10.7, 103.4 ± 11.2, 90.7 ± 8.3	2.4	3.9	18.5 (17.7)	6.4	61.7 ± 9.7

Table S4. Characteristic structural features of $A'_2FA_{n-1}Pb_nI_{3n+1}$ for n = 1,2 and 3. Octahedral tilting angles were measured with respect to two in-plane and one out-of-plane directions. Distances are given in Å. Dihedral angles of octahedral tilting angles and corresponding standard deviations are given in degrees.

n	Octahedral Tilting (°)	N···Pb (Å)	N···I (Å)	d_1(Å)	d_2(Å)
1	108.6 ± 15.4, 104.3 ± 7.7, -	3.0	3.9	17.9	6.5
2	90.8 ± 10.0, 93.4 ± 11.4, 89.1 ± 12.5	2.8	4.0	16.9	6.4
3	96.0 ± 8.7, 98.3 ± 6.9, 91.8 ± 13.1	2.8	4.0	18.6	6.4

S4.3. Electronic Properties

Electronic properties for the *n* = 1– 3 compositions of the RP phases of $A_2FA_{n-1}Pb_nI_{3n+1}$ and $A'_2FA_{n-1}Pb_nI_{3n+1}$ systems were calculated at PBE0 level including SOC effects (Tables S5–S6).

Table S5. Calculated band gaps (PBE0+SOC level) and hole/electron effective masses of $A_2FA_{n-1}Pb_nI_{3n+1}$ (*n* =1–3).

n	Band gap (eV)	$m_{h,xx}$ / $m_{e,xx}$	$m_{h,yy}$ / $m_{e,yy}$	$m_{h,zz}$ / $m_{e,zz}$
1	2.83, 2.4*	0.39 / 0.13	0.44 / 0.16	49 / 28
2	2.42	0.32 / 0.12	0.33 / 3.14	31 / 7.9
3	1.98	0.19 / 0.10	0.19 / 0.73	13 / 6.7

The asterisk indicates the experimental value.

Table S6. Calculated band gaps (PBE0+SOC level) and hole/electron effective masses of $A'_2FA_{n-1}Pb_nI_{3n+1}$ (*n*=1–3).

n	Band gap (eV)	$m_{h,xx}$ / $m_{e,xx}$	$m_{h,yy}$ / $m_{e,yy}$	$m_{h,zz}$ / $m_{e,zz}$
1	3.25	0.46 / 0.19	6.22 / 7.34	106 / 15
2	2.21	0.34 / 0.14	0.52 / 0.58	35 / 3.3
3	2.07	0.22 / 0.10	0.23 / 0.99	26 / 2.4

S4.4. Finite Temperature Properties

In order to assess the dynamics and thermo-structural stability of the organic-inorganic layered perovskite frameworks, we performed 5 ps of first-principles (DFT-based) Born-Oppenheimer molecular dynamics simulation of A_2PbI_4 and A'_2PbI_4 (Figures S10–S11).

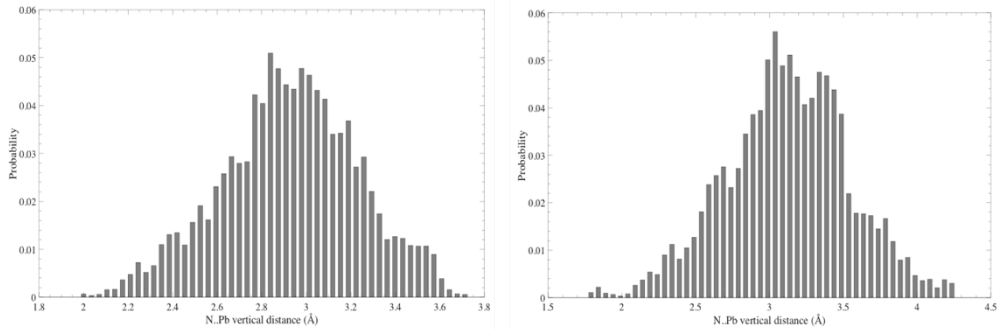

Figure S10. Penetration depth distribution of the N$\cdots$Pb distance for A_2PbI_4 (left) and A'_2PbI_4 (right).

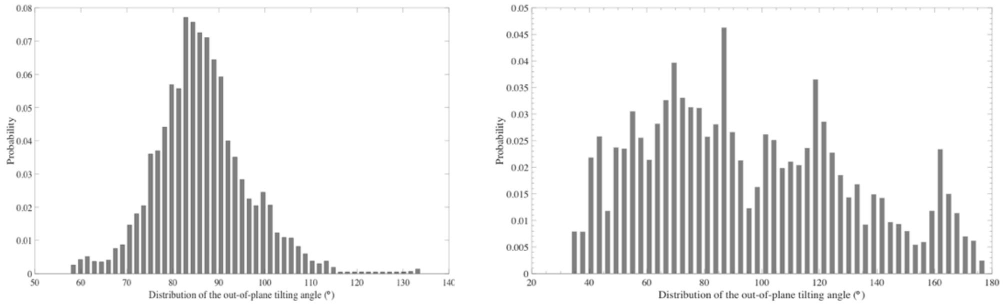

Figure S11. Distribution of the out-of-plane tilting angle for A_2PbI_4 (left) and A'_2PbI_4 (right).

S4.5. Stability

To assess the stability of $A_2FA_{n-1}Pb_nI_{3n+1}$ and $A'_2FA_{n-1}Pb_nI_{3n+1}$ (*n* = 1–3) representatives, we have calculated the corresponding formation enthalpies with respect to the reactants (PbI_2, FAI, and AI/A'I). The results are represented in Figure S12.

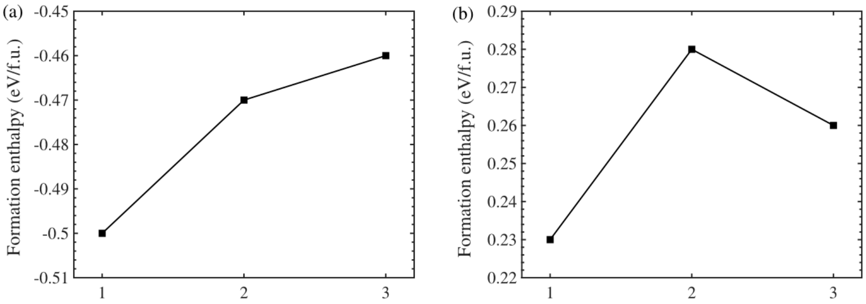

Figure S12. Formation energies of (a) $A_2FA_{n-1}Pb_nI_{3n+1}$ and (b) $A'_2FA_{n-1}Pb_nI_{3n+1}$ (*n* = 1–3).

S5. Time Resolved Microwave Conductivity Measurements

S5.1. Methods

Time-resolved microwave conductivity (TRMC) measurements were used to probe changes in conductivity of layered hybrid perovskites by using high frequency microwaves after the excitation by either high energy electron pulse or a laser.[20] The generated free charge carriers absorb part of the microwave power and the fraction of the incoming microwave power absorbed by the sample (ΔG) is proportional to the change in conductivity of the material ($\Delta\sigma$), which is defined as the product of charge mobility (μ) and quantum yield of free charge carrier formation (φ). Therefore, from the maximum change in conductivity ($\Delta\sigma_{max}$), mobility (μ) and quantum yield of free charge carrier formation (φ) can be obtained. The relative mobility of charge carriers was estimated by *pulse-radiolysis TRMC*. The samples prepared by *mechanosynthesis* were irradiated with short pulses of 3 MeV electrons from a Van de Graaff accelerator. *TRMC upon laser photoexcitation* under conditions specified in the corresponding figure captions was used to analyse *thin films* of approximately 200 nm thickness of the layered perovskite materials based on different composition (*n* = 1–3).

S5.2 Supplementary Spectral Data

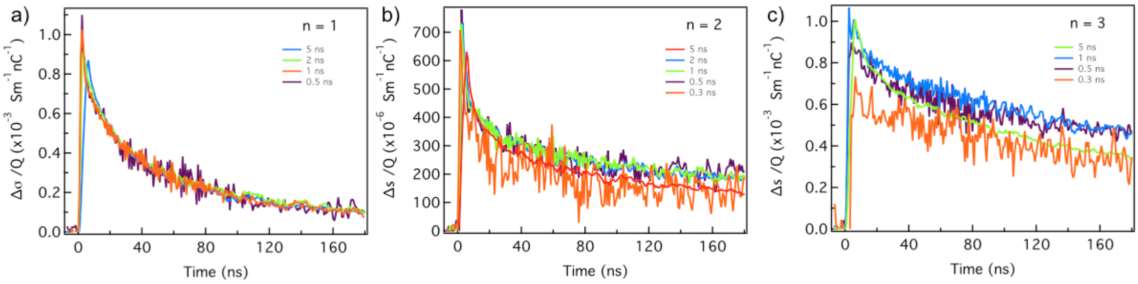

Figure S13. Charge carrier dynamics in $A_2FA_{n-1}Pb_nI_{3n+1}$ perovskite powders of *n* = 1–3 compositions. Evolution of the conductivity as a function of pulse length at 293 K. The initial concentration of charge carriers is found to be in the order of 10^{14} to 10^{16} cm^{-3}.

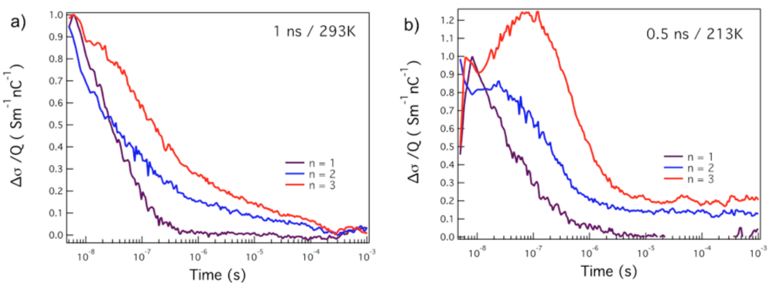

Figure S14. Normalized conductivity in $A_2FA_{n-1}Pb_nI_{3n+1}$ perovskite powders for various *n* = 1–3 compositions over time at (a) 1 ns pulse length (293 K) and (b) 0.5 ns pulse length (213 K).

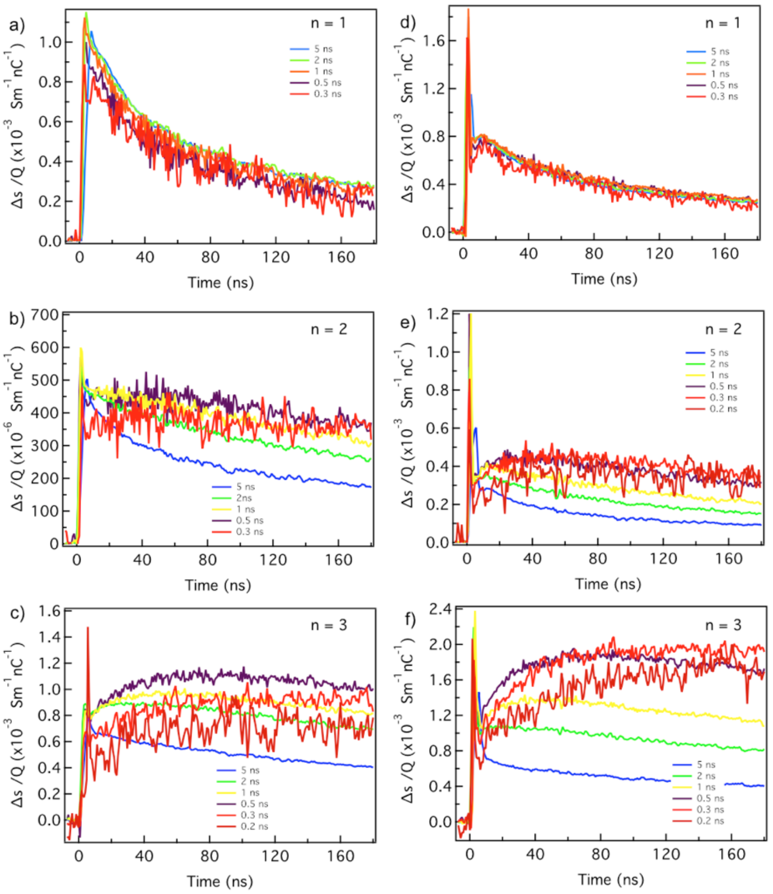

Figure S15. Evolution of conductivity in $A_2FA_{n-1}Pb_nI_{3n+1}$ perovskite powders for *n* = 1–3 compositions over time at various pulse lengths (ns) at (a–c) 213 K and (d–f) 153 K. The initial concentration of charge carriers is found to be in the order of 10^{14} to 10^{16} cm^{-3}.

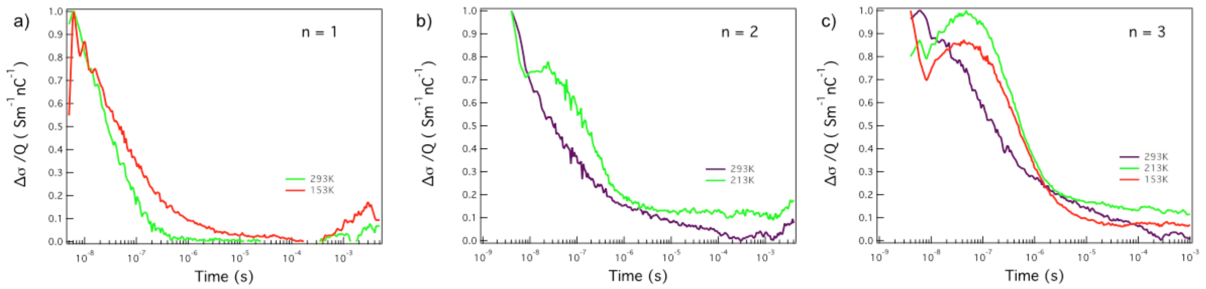

Figure S16. Charge carrier dynamics in $A_2FA_{n-1}Pb_nI_{3n+1}$ perovskite powders of *n* = 1–3 compositions. Evolution of conductivity as a function of temperature (153 K, 213 K, and 293 K) at 1 ns pulse length. The initial concentration of charge carriers is found to be in the order of 10^{14} to 10^{16} cm^{-3}.

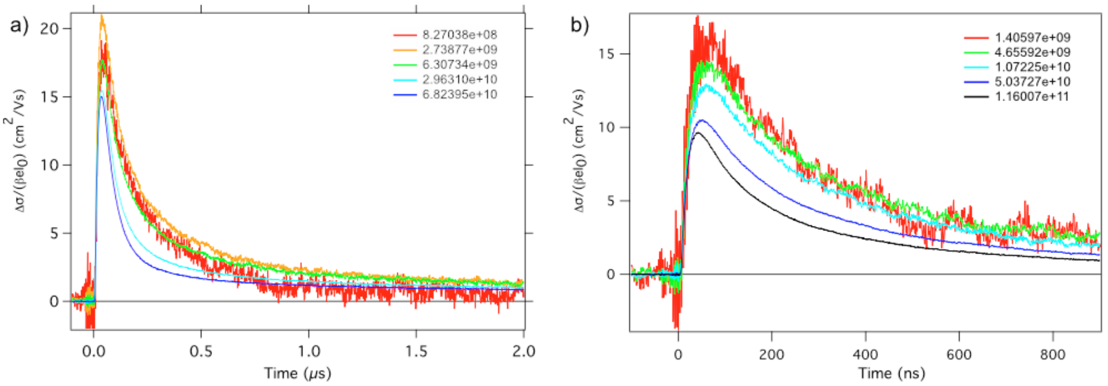

Figure S17. Evolution of photoconductivity of FAPbI$_3$ prepared by (a) solution deposition and (b) evaporation over time as a function of photon intensity (cm^{-2}) at 293 K upon laser excitation at 650 nm.

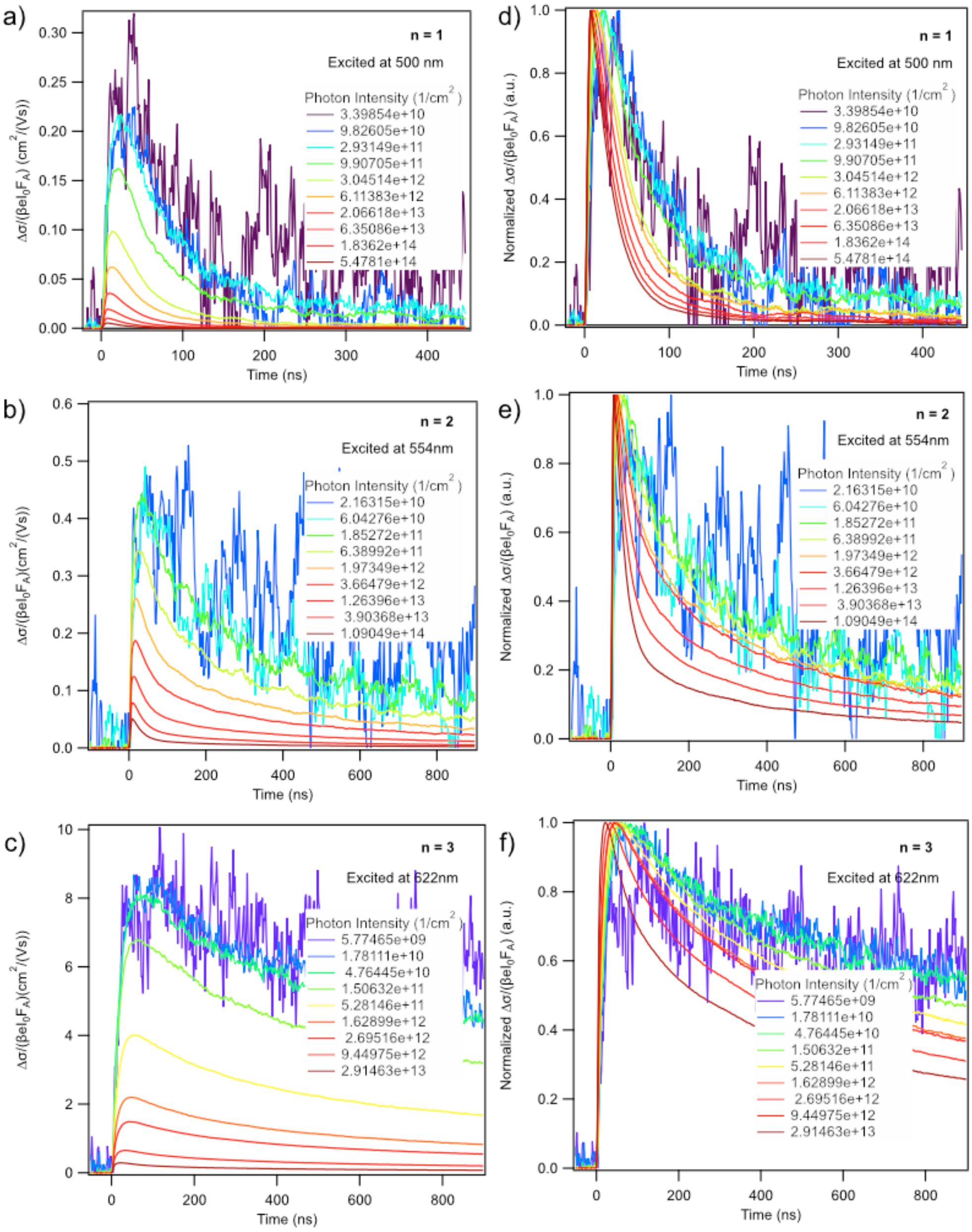

Figure S18. Evolution of photoconductivity in A$_2$FA$_{n-1}$Pb$_n$I$_{3n+1}$ perovskite films of n = 1–3 compositions over time upon excitation by various photon intensities (cm^{-2}) at 293 K for (a) *n* = 1 (excitation at 500 nm), (b) *n* = 2 (excitation at 567 nm), and (c) *n* = 3 (excitation at 622 nm) compositions. (d–f) Normalized transients.

References

[1] D. Prochowicz *et al.*, Mechanoperovskites for Photovoltaic Applications: Preparation, Characterization, and Device Fabrication. *Acc. Chem. Res.* **52**, 3233–3243 (2019)

[2] D. J. Kubicki *et al.*, Cation Dynamics in Mixed-Cation $(MA)_x(FA)_{1-x}PbI_3$ Hybrid Perovskites from Solid-State NMR. *J. Am. Chem. Soc.* **139**, 10055–10061 (2017)

[3] J. V. Milić *et al.,* Supramolecular Engineering for Formamidinium-Based Layered 2D Perovskite Solar Cells: Structural Complexity and Dynamics Revealed by Solid-State NMR Spectroscopy. *Adv. Energy Mater.* **9**, 1900284 (2019)

[4] K. Momma and F. Izumi, VESTA 3 for Three-Dimensional Visualization of Crystal, Volumetric and Morphology Data, *J. Appl. Crystallogr.* **44**, 1272–1276 (2011)

[5] C. Caddeo *et al.,* Collective Molecular Mechanisms in the $CH_3NH_3PbI_3$ Dissolution by Liquid Water. *ACS Nano* **11**, 9183–9190 (2017)

[6] J.-P. Ryckaert *et al.*, Numerical Integration of the Cartesian Equations of Motion of a System with Constraints: Molecular Dynamics of *n*-Alkanes. *J. Comput. Phys.* **23**, 327–341 (1977)

[7] S. Plimpton, Fast Parallel Algorithms for Short-Range Molecular Dynamics. *J. Comput. Phys.* **117**, 1–19 (1995)

[8] G. Bussi, D. Donadio, and M. Parrinello, Canonical Sampling through Velocity Rescaling. *J. Chem. Phys.* **126**, 014101 (2007)

[9] M. Parrinello and A. Rahman, Polymorphic Transitions in Single Crystals: A New Molecular Dynamics Method. *J. Appl. Phys.* **52**, 7182–7190 (1981)

[10] W. Humphrey, A. Dalke, and K. Shulten, VMD: Visual Molecular Dynamics. *J. Mol. Graphics* **14,** 33–38 (1996).

[11] P. Giannozzi *et al.*, QUANTUM ESPRESSO: A Modular and Open-Source Software Project for Quantum Simulations of Materials. *J. Phys.: Condensed Matter* **21**, 395502–395502 (2009)

[12] J. P. Perdew *et al.*, Restoring the Density-Gradient Expansion for Exchange in Solids and Surfaces. *Phys. Rev. Lett.* **100**, 136406–136406 (2008)

[13] N. Ashari-Astani *et al.*, Ruddlesden–Popper Phases of Methylammonium-Based Two-Dimensional Perovskites with 5-Ammonium Valeric Acid $AVA_2MA_{n-1}Pb_nI_{3n+1}$ with n = 1, 2, and 3. *J. Phys. Chem. Lett.* **10***,* 3543–3549 (2019)

[14] A. Q. Alanazi *et al.*, Atomic-Level Microstructure of Efficient Formamidinium-Based Perovskite Solar Cells Stabilized by 5-Ammonium Valeric Acid Iodide Revealed by Multi-Nuclear and Two-Dimensional Solid-State NMR. *J. Am. Chem. Soc.* **141**, 17659–17669 (2019)

[15] S. Grimme, Semiempirical GGA-Type Density Functional Constructed with a Long-Range Dispersion Correction. *J. Comput. Chem*. **27**, 1787−1799 (2006)

[16] P. Umari *et al.*, Relativistic GW Calculations on $CH_3NH_3PbI_3$ and $CH_3NH_3SnI_3$ Perovskites for Solar cell Applications. *Sci. Rep.* **4**, 4467–4467 (2014)

[17] J. Wiktor *et al.*, Predictive Determination of Band Gaps of Inorganic Halide Perovskites. *The J. Phys. Chem. Lett.* **8**, 5507–5512 (2017)

[18] N. Ashari-Astani *et al.* Computational Characterization of the Dependence of Halide Perovskite Effective Masses on Chemical Composition and Structure. *J. Phys. Chem. C* **121,** 23886–23895 (2017).

[19] S. Ahmad *et al.*, Dion-Jacobson Phase 2D Layered Perovskites for Solar cells with Ultrafast Stability, *Joule* **3**, 794–806 (2018)

[20] R. Herckens *et al.*, Multi-Layered Hybrid Perovskites Templated with Carbazole Derivatives: Optical Properties, Enhanced Moisture Stability and Solar Cell Characteristics. *J. Mater. Chem. A*. **6**, 22899–22908 (2018)